

The development of high-speed particle image velocimetry (20 kHz) for large eddy simulation code refinement in bluff body flows

T.C. Williams, G.K. Hargrave, N.A. Halliwell

Abstract Flow interaction with a bluff body generates a highly complex flow field and has been the subject of much experimental and theoretical analysis. It has been shown that large eddy simulation (LES) modelling provides a more realistic analysis of the flow for such situations where the large scales of turbulence must be resolved. The inherent small-scale spatial velocity averaging in particle image velocimetry (PIV) is commensurate with the sub-grid scale modelling of LES and, therefore, offers potential as a code refinement technique. To demonstrate this potential, however, PIV must be performed with a temporal resolution of typically kHz and a spatial resolution of sub-mm² to be relevant for the vast majority of flows of engineering interest. This paper reports the development of a high-speed PIV system capable of operating at 20 kHz with a spatial resolution of 0.9 mm². This is the combined highest speed, highest resolution PIV data reported to date. The experiment chosen to demonstrate the system is the study of the steady flow interaction with circular and square cross-section obstacles. A Reynolds number of 3,900 is chosen for the cylinder flow to extend the database used by Breuer M. (1998 *Int J Heat Fluid* 19:512–521) in his extensive LES modelling of this flow. Data presented include a sequence of two-dimensional velocity and vorticity fields, including flow streamlines. Importantly, the random error, inherent in a PIV measurement, is discussed and a formula presented which allows the error to be estimated and regions of the flow identified where LES comparisons would be uncertain.

1 Introduction

Flow interaction with bluff bodies is of interest in many areas of engineering, including: wind interactions with external structures, such as buildings or chimneys, flows over heat exchanger tubes in boilers and vehicle aerodynamics. Achieving a complete understanding of the physical processes provides many challenging problems in

terms of both experimental measurement and theoretical analysis. To facilitate the development and validation of predictive computational fluid dynamics (CFD) codes for the analysis of highly turbulent flow fields, experimental data are required in situations with large spatial and temporal velocity gradients. The experimental challenge lies in the acquisition of high temporal (several kHz) and high spatial (sub-mm²) resolution data. This paper describes the development and application of a time-resolved particle image velocimetry (PIV) system incorporating high-speed, high-resolution image recording to quantify the temporal evolution of turbulent structures in the wake of bluff body obstacles.

For steady flow around bluff bodies, most calculations found in the literature are based on the Reynolds-averaged Navier–Stokes (RANS) equations. The flow past bluff bodies generates a complex flow field with periodic eddy shedding, which forms large-scale vortices in the obstacle wake. Depending on the obstacle geometry and flow Reynolds number, the wake flow becomes asymmetric and unsteady. With eddy shedding from bluff bodies, it is necessary to apply the unsteady RANS equations to define the periodic vortex generation, and turbulence models are used to superimpose the stochastic turbulent fluctuations. The many incarnations of the k - ϵ model have been used with varying degrees of success. Rodi et al. (1997, 1998) showed that RANS calculations with statistical turbulence models do not generate good predictions for flow situations with large-scale, unsteady vortices.

As discussed by Rodi et al. (1997), large eddy simulation (LES) modelling provides a more realistic analysis of the flow around bluff body obstacles. Computationally, LES is a more intensive scheme, but allows the large-scale unsteady motion to be resolved. There have been many experimental studies into the structure of the near wake of various cross-sectioned obstacles exposed to a steady cross flow. Cantwell and Coles (1983) provided phased-averaged data for velocities and stresses for flows around circular cylinders using a flying hot wire system. By applying laser Doppler velocimetry (LDV), Lyn et al. (1994, 1995) extended this study to the flow around a square cross-section obstacle, providing phase (ensemble)-averaged velocities and turbulence intensities for high Reynolds number flows. Qualitatively, the main flow features observed for the square cross-section were essentially the same as those for the cylinder. However, detailed quantitative comparison revealed significant differences. The length scales of eddies in the obstacle wake were larger for the square cross-section case, and peak values for both turbulence

Received: 10 October 2002 / Accepted: 14 February 2003
Published online: 21 June 2003
© Springer-Verlag 2003

T.C. Williams, G.K. Hargrave, N.A. Halliwell (✉)
Wolfson School of Mechanical and Manufacturing Engineering,
Loughborough University, Loughborough,
Leicestershire, LE11 3TU, UK
E-mail: N.A.Halliwell@lboro.ac.uk

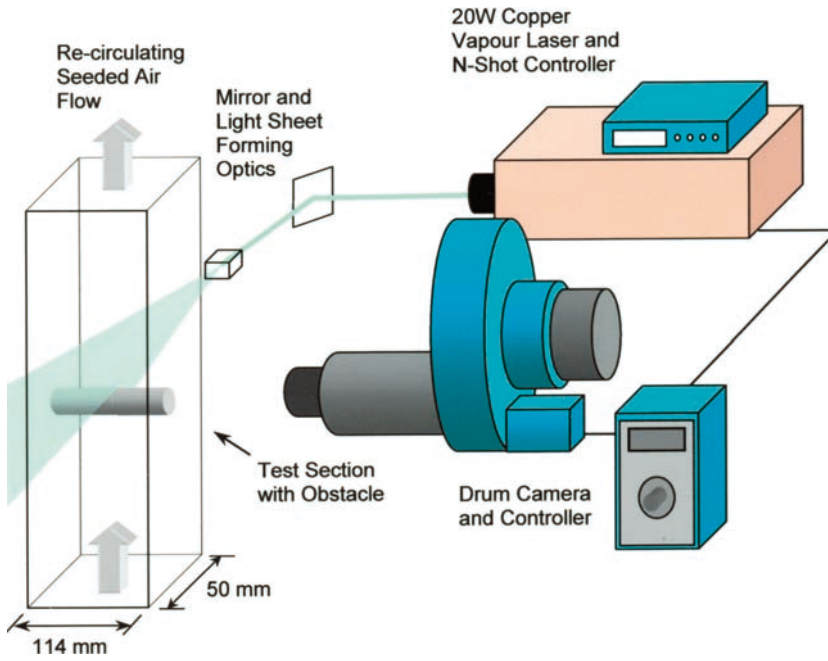


Fig. 1. A schematic of the time-resolved PIV system and steady-flow test rig

and periodic stresses were significantly higher in the wake of the square obstacle compared with the cylinder.

The most extensive large eddy simulation of the flow past a circular cylinder was carried out by Breuer (1998) for a flow Reynolds number (Re) of 3,900. Comparisons were made between the computed LES and the mean velocity along the centre line of the cylinder. The experiment reported in what follows was chosen to extend the database for flow around circular obstacles at $Re=3,900$ to complement the LES modelling work of Breuer (1998). Sequences of high-resolution PIV images in the wake of both circular and square cross-sectioned obstacles were captured. The capture rate of 20 kHz was easily sufficient to time-resolve the development of the eddy formation in the near wake and provided a high-resolution data set for the validation of LES models.

2 Experimental facility and diagnostics

2.1 Experimental rig and seeding considerations

The steady flow experimental rig consisted of circular and square cross-section rods subjected to a uniform cross flow. The experiments were conducted in a recirculating wind tunnel with a cross-section of 50 mm×114 mm. The tunnel was driven by axial fans, and the flow velocity was monitored using a calibrated hot-wire anemometer. For the results presented in this paper, the stream velocity (U_∞) was maintained at 6.8 m/s. The particulate seeding used for the PIV was olive oil droplets generated using an air-assisted atomiser. The mean particle size was 1 micron. These droplets were small enough to accurately follow flow fluctuations to a frequency of 10 kHz (Durst et al. 1982). A major advantage of the recirculating tunnel was that the seeding particle density could be carefully controlled to optimise the acquisition of high spatial resolution data in the PIV system. Seeding density is the fundamental

parameter which dictates spatial resolution in a PIV measurement. In order to generate a reproducible seeding level, until the optimum was achieved, a monitor system was mounted in the return section of the tunnel. This consisted of a helium–neon laser and a photodiode detector, which was used to measure the relative obscuration of the laser beam over a path length of 2 m. This simple monitoring system was the key to the sub- mm^2 resolution achieved in the experiments. A series of trial and error experiments calibrated the system and, consequently, in an actual experimental test, the PIV images were recorded at the optimum seeding density to ensure high-quality data.

Experimental data for flow around a cylinder with diameter $d_c=8$ mm and a square cross-section rod with side length $d_s=8$ mm were obtained. The rods were mounted in the centre of the tunnel across the longer side. The Reynolds number was 3,900, based on U_∞ and the obstacle characteristic dimension, and the eddy shedding frequency, based on a Strouhal number of 0.2, was calculated to be 168 Hz.

2.2 The time-resolved PIV system

Figure 1 shows a schematic of the time-resolved PIV system installed on the steady-flow rig. A copper vapour laser was used to produce the laser illumination necessary for the PIV technique. Over the range of frequencies used in this study, the laser generated approximately 2 mJ per pulse. A laser sheet approximately 500 μm thick was formed using a bi-convex spherical lens (focal length=1.5 m) and a plano-convex cylindrical lens (focal length=0.2 m). This was introduced into the test section through the wide walls of the wind tunnel and orientated so as to both bisect the length of the cylinder and to be perpendicular to its long axis.

The laser light scattered from the olive oil droplets was recorded using a drum camera recording with 35 mm

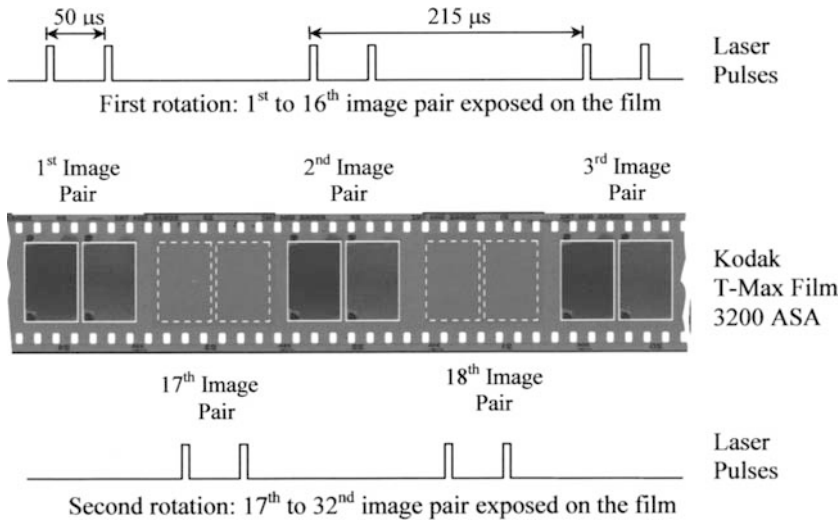


Fig. 2. An example of the novel PIV recording process. With a drum film speed of 300 m/s, the copper vapour laser is triggered to produce pairs of light pulses. Complete separation of the PIV image pairs is achieved and, by interlacing the PIV image pairs, the recording process continues over two drum rotations

Kodak T-max (3200 ASA) film. The camera was operated with a film mask size of 14.5×24 mm and a magnification of 0.5. The imaging lens was a 105 mm macro lens, operated at $f/8$, which produced particle images in the film plane diffraction limited to 15.5 μm. The depth-of-field of the imaging optics was 1.3 mm, which is wider than the laser sheet thickness, thereby ensuring accurate focus of all illuminated particles. The camera drum was rotated at the maximum speed of 300 rev/s, producing an effective film speed of 300 m/s. A laser control unit, synchronised to the camera shutter, generated consecutive laser pulses at a separation of 50 μs. This produced a continuous sequence of 66 separate PIV images, which were cross-correlated to give time-resolved PIV at 20 kHz.

In this continuous recording approach, the total recording time was limited by the length of film contained within the drum, 1 m of film giving 3.3 ms for a mask width of 14.5 mm. For many applications, it is important to extend the recording time to capture sequences of PIV exposure pairs at a lower repetition frequency, while maintaining the short time separation between each exposure. This allows the recording of the temporal variance of a low-frequency event occurring in a high-velocity flow field. In a previous study, Köhler et al. (1993) demonstrated the application of time-resolved PIV to the study of in-cylinder flow in a diesel engine. In their work, PIV exposure pairs were collected at a rate of 200 Hz. With a drum speed of 5 m/s, exposure pairs were recorded with a laser pulse separation of 33 μs. This low drum speed produced overlaid exposures on the film, and these were analysed by auto-correlation processing. In their study, directional ambiguity was avoided due to the particle image shift introduced by the film translation. A disadvantage of the autocorrelation PIV processing employed by Köhler et al (1993) is the increase in mean noise level and the inherent reduction in dynamic range (Reeves et al. 1996).

Cross correlation avoids this problem and, in the present study, it was achieved by an approach similar to that presented by Lecordier and Trinité (1999) in a time-resolved PIV study of a turbulent premixed flame at 6.8 kHz. Complete exposure separation, while operating at

a lower repetition frequency, was maintained. This was accomplished by operating the drum camera at its maximum speed of 300 rev/s and recording the PIV sequence over several rotations of the drum. The laser control unit was configured to generate 50-μs pulse pairs at a variable repetition frequency. This flexibility in the control of the pulse-pair frequency allowed the exposure pairs to be exposed on to the film at any time interval. An example of the image recording process is described in Fig. 2. In this case, the pulse-pair repetition frequency of the laser was set to 4,650 Hz. On the first drum rotation, a total of 16 exposure pairs were recorded on the 1 m length of film; each exposure in a pair being separated by 50 μs and the pairs separated by 215 μs. With this choice of repetition frequency, on the second rotation of the drum the exposure pairs were interlaced between the pairs recorded on the first rotation. Clearly, by careful selection of the repetition frequency, it is possible to extend the total recording time over several drum rotations, while maintaining a time interval between PIV exposure pairs of 50 μs.

This mode of operation is extremely useful for providing data for LES simulations of flow over bluff bodies, since repetition frequency can be tailored to the time step required to capture the eddy shedding process. The only limitations to this approach are the practical problems associated with maintaining constant laser pulse energy and drum speed. In the current study, the sequence of PIV exposures were photographically printed at 150×250 mm and digitised to a resolution of 2140×3170 pixels. This gave an ultimate resolution in the film plane of 7.5 μm/pixel and, with a diffraction limited spot size of 15.5 μm, this ensured that, in the final digitisation, each particle image occupied at least 4 pixels; an essential criterion for sub-pixel determination of the correlation peak location and prevention of peak-locking effects (Raffel et al. 1998). In the present study, the location of the correlation peak was determined using a multi-point interpolation routine, giving a sub-pixel resolution of 0.1 pixel (Lorrenco and Krothapalli 1994).

Since each particle field image was digitised from the film separately, it was essential to accurately align the two

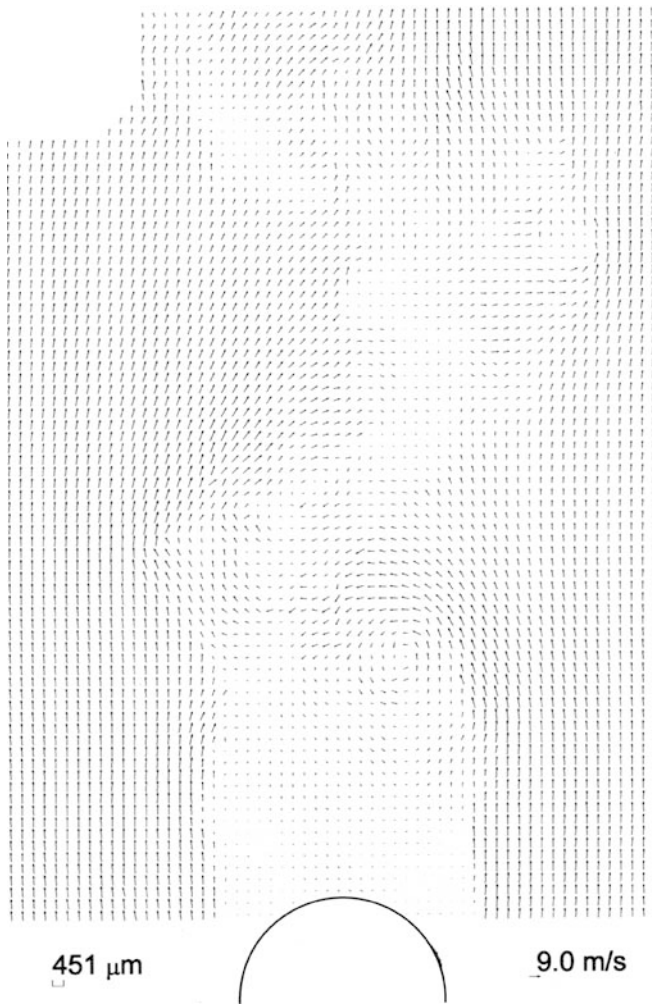


Fig. 3. Time-resolved PIV imaging of flow in the wake of a cylindrical obstacle

images prior to the cross-correlation analysis. Two registration marks were recorded on adjacent corners of each image frame using an optical fibre, which sampled from the laser source. Subsequent cross-correlation of the registration marks provided alignment to a sub-pixel resolution comparable with the PIV analysis. With two physically separated registration marks, both translational and rotational alignment accuracy were maintained. Cross-correlation analysis of consecutive exposure pairs was based on a 50% overlap of 64×64 pixel window, providing a spatial resolution of 0.9 mm^2 in the flow.

3 Results and discussion

3.1 Experimental results

An example PIV velocity vector map of the flow field in the wake of a cylindrical obstacle is presented in Fig. 3. The PIV data presented in this figure were validated using a maximum velocity threshold and a vector continuity routine, with predefined limitations on the absolute vector-to-vector velocity gradients and allowable angular

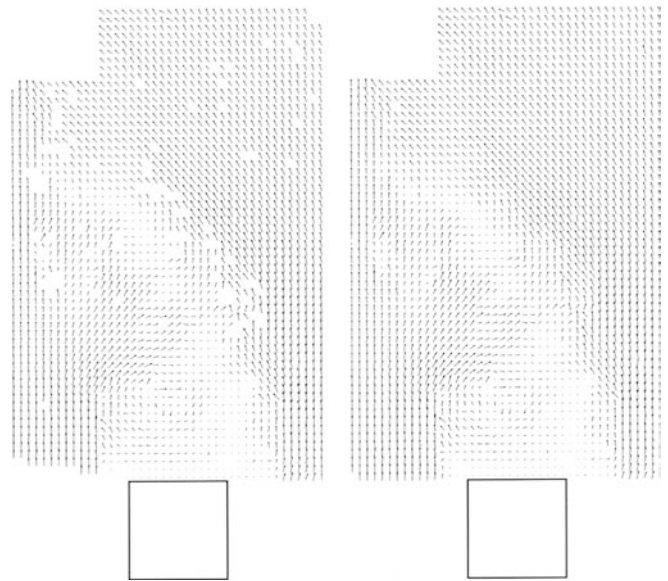


Fig. 4. PIV images showing the velocity field in the wake of a square cross-sectioned obstacle. The *left-hand image* shows the velocity field after validation. The *right-hand image* shows the same velocity field with the gaps interpolated

variation. Within the validation, any erroneous first correlation peaks were substituted with second and then third correlation peaks in an attempt to find a satisfactory vector. If these correlation peaks also failed, the validation the vector was deleted. Any gaps in the vector field were then subsequently filled using a multi-point polynomial interpolation routine. The PIV velocity maps presented in Fig. 4 illustrate this procedure. The map shows the wake region behind a square cross-sectioned obstacle. The left-hand vector field shows the velocity field after validation. Five per cent of the vectors have been deleted. Of the remaining vectors, 91% are first correlation peaks. The reasons for loss of valid velocity vectors are directly attributed to out of plane motion and severe velocity gradients. The loss of data due to severe velocity gradients is evidenced in Fig. 4 along the right-hand diagonal boundary between the main flow and the eddy region. The right-hand map in Fig. 4 shows the velocity field after the velocity vector gaps have been filled.

The PIV data presented in Fig. 3 demonstrate the high spatial resolution that can be achieved using the current system operating at a collection rate of 20 kHz. The wake region is visible downstream of the obstacle, with a strong eddy rotation on the right-hand side. Since, with the current configuration the drum camera was operating at its maximum speed, it is only possible to increase the collection rate by decreasing both the exposure mask width and the exposure-pair separation time. The result of this is either a decrease in the imaged flow area or, if the imaged flow area is maintained, a change in magnification, in which case the flow resolution is reduced. Another aspect of operating at increasing collection rates is a decrease in laser pulse energies, which reflects directly on image quality. The attained speed of 20 kHz is the fastest PIV reported to date and is sufficient for most flows of engineering interest.

The key factor in obtaining high-quality PIV data is the quality of the particle images and the seeding density control. The final particle image size on the recording 35 mm film was limited by diffraction to 15.5 μm and the seeding density was carefully controlled to produce approximately 40 particle images per interrogation region. This high image density is fundamental in ensuring that the signal to noise ratio of the correlation peak, in comparison with noise peaks in the correlation plane, is optimised (Lawson et al 1997). Much experimental effort was expended to ensure that the seeding level remained constant throughout the entire imaged region of the flow, as discussed earlier. The aim was to ensure that the rapid rotation and high-velocity gradients in the wake of the obstacles did not cause particle image density changes.

3.2

Measurement uncertainty

In order to have confidence in the use of high-speed PIV data for LES code refinement, it is necessary to consider the measurement uncertainty associated with the experimental technique. The overall measurement accuracy of a PIV system is a combination of a variety of aspects from the recording process itself through to the choice of a correlation peak and the method chosen to measure its position (Raffel et al. 1998). For the purposes of this paper, it is helpful to distinguish between correlation errors associated with the detection of a valid velocity vector in an interrogation region and the inherent random error in this measurement. The correlation errors were minimised by optimising the seeding density and particle image resolution and were estimated at typically 3% in a worst case. The random error is associated with a valid vector representing a sample of the velocity field (commensurate with the size of the interrogation region chosen) and arises due to the random position of the seeding particle images in the presence of a velocity gradient in the region. The rms error σ_E is given by:

$$\sigma_E = \frac{L}{|V_0|\sqrt{12N}} \left[\left[\frac{\partial u}{\partial x} \right]^2 + \left[\frac{\partial u}{\partial y} \right]^2 + \left[\frac{\partial v}{\partial x} \right]^2 + \left[\frac{\partial v}{\partial y} \right]^2 \right]^{\frac{1}{2}} \quad (1)$$

where $|V_0|$ is the velocity at the centre of a square interrogation region of side length L , and N is the number of paired particle images in the region. The components of velocity in the direction of the mean flow and normal to the cylinder axis are u, v respectively. This formula was developed by Lawson (1995) based on a model of a PIV experiment and verified by a Monte Carlo simulation. In the present study, the errors were estimated by calculating the velocity gradients across neighbouring interrogation regions and using a value of $N=40$.

Figure 5 shows the error distribution across the flow field. The mean error was calculated to be 2.6%, and the high values are clearly seen to be associated with the regions of severe velocity gradients. The random error in these regions is in excess of 15%. Bolinder (2000) studied random errors in a round jet flow at $Re=5,800$. The random errors estimated by the Lawson formula given by Eq. (1) agree with the estimates from this work for similar high-velocity gradients across a 64×64 pixel interrogation

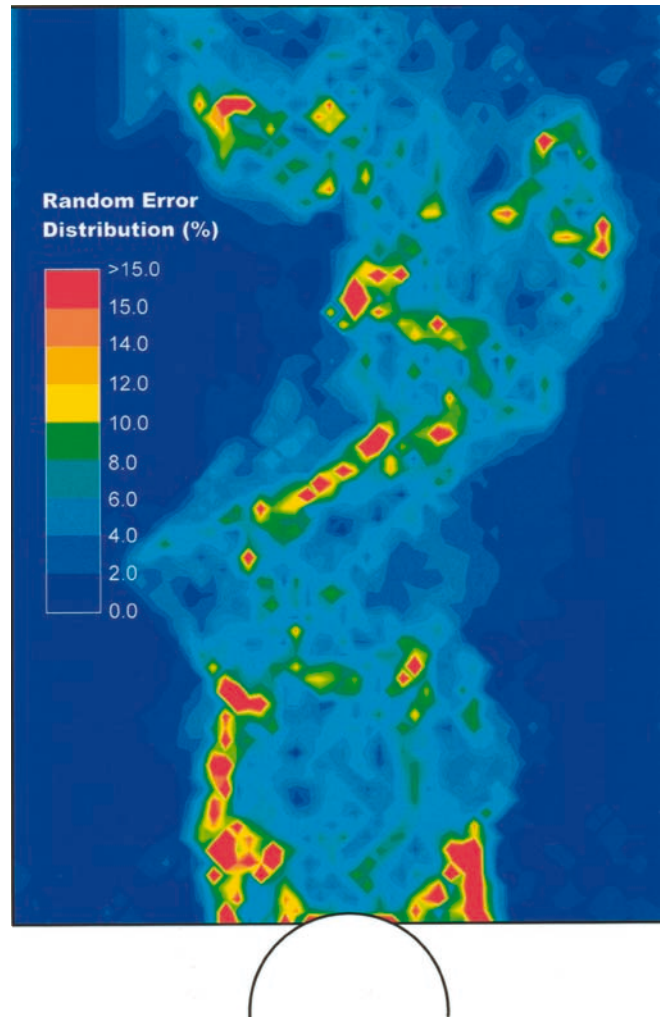


Fig. 5. Distribution of the random error corresponding to the PIV vector field result presented in Fig. 3

region. These errors can be reduced by re-analysing the particle image data with a reduced interrogation region size. Bolinder (2000) attempted 8×8 interrogation regions but pointed out this approach is limited due to an insufficient particle image density for this size, which prevents detection of a valid correlation peak. There is a trade-off between interrogation region size, particle image pixel resolution and the dynamic range of a PIV system (Lawson et al 1997). For the purposes of this paper, a choice of 64×64 pixels, providing a spatial resolution in the flow field of 0.9 mm^2 , was optimal.

3.3

Time evolution of the flow

To illustrate the data set obtained during this study, a sequence of five instantaneous flow maps for the flow past the cylindrical obstacle are displayed in Fig. 6. The vector maps are presented in terms of velocities relative to a stationary observer and include streamlines superimposed on the vector field to highlight the eddy formation and convection. At time zero, a large eddy is located on the left side of the wake region with a smaller one forming below it and to the right. As the sequence progresses, the larger

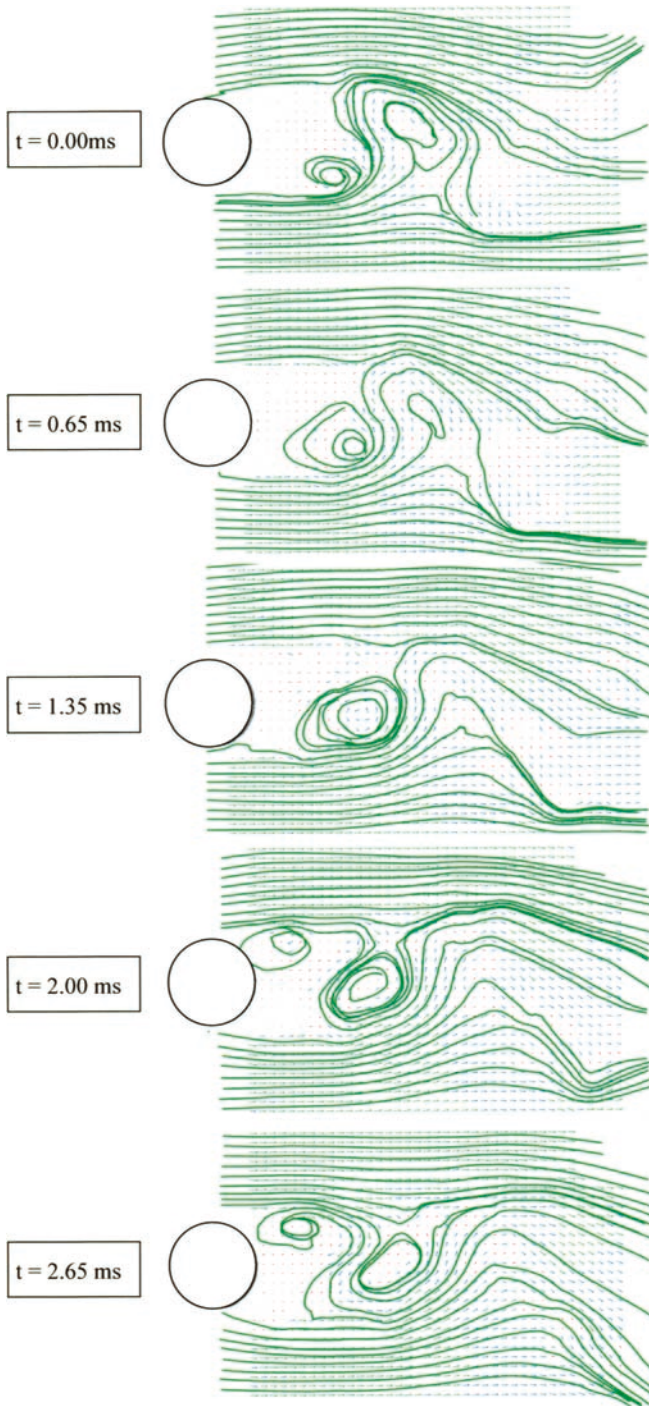


Fig. 6. A sequence of PIV velocity maps with flow streamlines overlaid to highlight the development of the flow structures in the wake of the cylindrical obstacle

eddy decays and the smaller one grows in strength as it convects downstream. Towards the end of the cycle, the next eddy can be seen starting to form on the left of the cylinder. The sequence represents approximately half an eddy-shedding cycle for this flow field, providing confirmation of the estimated shedding frequency based on a Strouhal number of 0.2.

Figure 7 shows vorticity plots corresponding to the flow sequence presented in Fig. 6, with positive and negative vorticity represented by red and blue regions respectively.

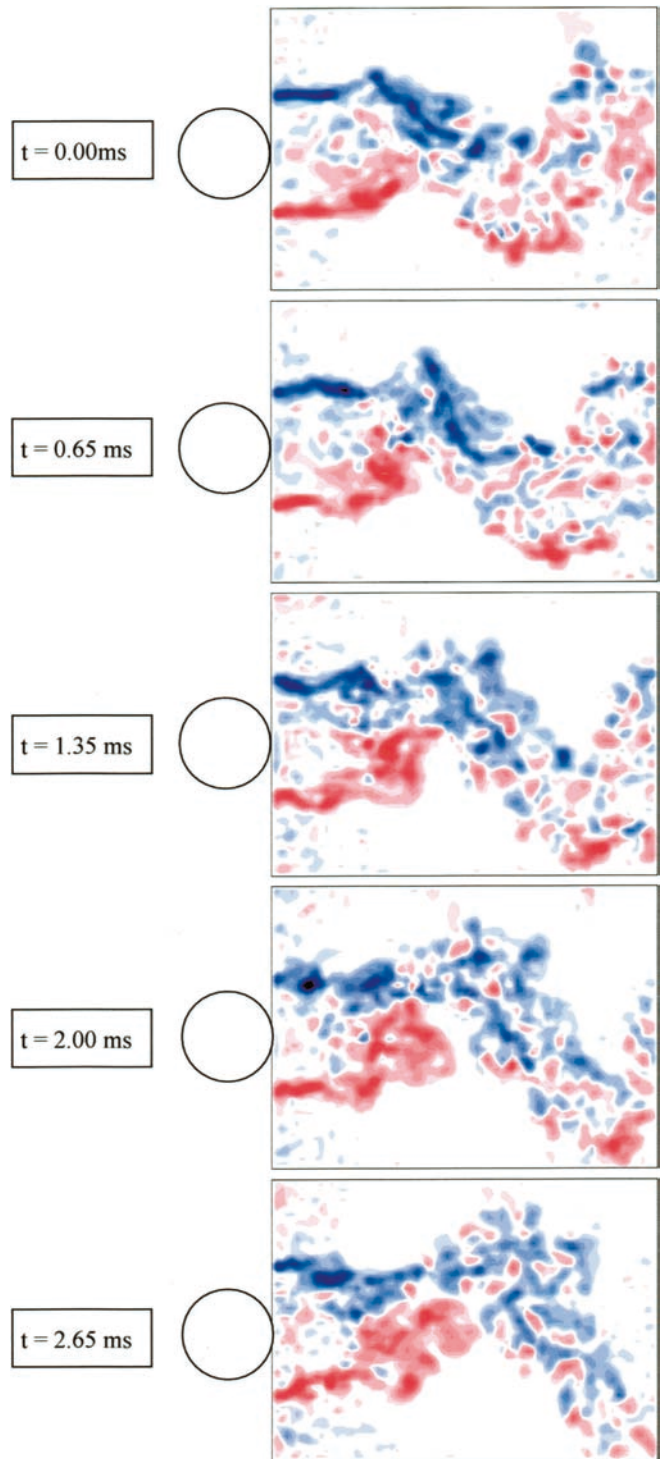


Fig. 7. Plots of vorticity calculated from the velocity fields presented in Fig. 6

As expected, directly downstream of the obstacle, there are high levels of vorticity corresponding to the two shear layers. The vorticity sequence shows how these layers roll up asymmetrically to form the classic eddy shedding pattern. Initially, in the sequence, a large region of negative vorticity is present on the left-hand side. The presence of this structure causes “roll-up” of the flow and the generation of bulk rotation on the opposing side of the wake region. This is evident in the vorticity sequence with the

build-up in both intensity and size of the positive (red) vorticity region between one and two diameters downstream of the obstacle.

At approximately two diameters downstream of the obstacle, there is a distinct point where the large vorticity structures break down into smaller scales. This occurs at the interaction between the flows from the opposing eddy structures. It is interesting to note that, even at four diameters downstream of the cylinder, there are still distinct regions of high vorticity gradients with both positive and negative vorticity present.

4

Conclusions

This paper has demonstrated the potential of high-speed PIV as an LES code refinement technique. A time-resolved PIV system was developed which can provide velocity imaging at 20 kHz with a spatial resolution of 0.9 mm^2 . The experiments examined flows in the wake of bluff bodies and, in particular, extended the data set for flow past a circular cylinder at a Reynolds number of 3,900, commensurate with the LES modelling of Breuer (1998). Great effort was needed to control the seeding density in the experiments to ensure both diffraction-limited imaging and a high image density. Only in the regions of very high-velocity gradients did the first choice of a correlation peak fail to produce a valid sector. Having achieved a complete velocity vector map, we presented a consideration of measurement uncertainty. The random error, inherent in PIV measurements, in the presence of high-velocity gradients was considered. A formula was presented which allows for straightforward estimation of this error, and these predictions were in agreement with the work of Bolinder (2000). The highest error in the regions of severe velocity gradients was in excess of 15%. The mean random error across the whole flow field was calculated at less than 3%.

The high spatial resolution velocity data allowed the computation of the out-of-plane vorticity. With the temporal resolution achieved with this PIV system, the

vorticity results, combined with the velocity data, allowed for the temporal development and interaction of individual eddy cycles to be tracked and understood.

References

- Bolinder J (2000) In situ estimation of the random error in DPIV measurements. In: The Proceedings of the 9th International Symposium on Flow Visualisation CDROM Proceedings (ISBN 0 9533991-1-7). Heriot-Watt University, Edinburgh
- Breuer M (1998) Numerical and modelling influences on large-eddy simulations for the flow past a circular cylinder. *Int J Heat Fluid* 19:512–521
- Cantwell B, Coles D (1983) An experimental study of entrainment and transport in the turbulent near wake of a circular cylinder. *J Fluid Mech* 136:321–374
- Durst F, Melling A, Whitelaw JH (1982) Principles and practice of laser doppler anemometry. Academic Press, New York
- Köhler J, Lawrenz W, Meier F, Meinhardt P, Stolz W, Bloss WH (1993) Flow field diagnostics in industrial devices. *Ber Bunsenges Phys Chem* 7:1568–1573
- Lawson NJ (1995) The application of particle image velocimetry to high speed flows. PhD Thesis, Loughborough University
- Lawson NJ, Halliwell NA, Coupland JM (1997) A generalised optimisation method for double pulsed particle image velocimetry. *Opt Lasers Eng* 27:656–673
- Lecordier B, Trinité M (1999) Time-resolved PIV measurements for high-speed flows. Third International Workshop on Particle Image Velocimetry, Santa-Barbara, Calif.
- Lorenzo L, Krothapalli A (1994) On the accuracy of velocity and vorticity measurements with PIV. *Exp Fluids* 18:421–428
- Lyn DA, Rodi W (1994) The flapping shear layer formed by flow separation from the forward corner of a square cylinder. *J. Fluid Mech* 267:353–376
- Lyn DA, Einav S, Rodi W, Park J-H (1995) A laser-Doppler velocimetry study of ensemble-averaged characteristics of the turbulent near wake of a square cylinder. *J Fluid Mech* 304:285–319
- Raffel M, Willert C, Kompenhans J (1998) Particle image velocimetry: a practical guide. Springer, Berlin Heidelberg New York
- Reeves M, Garner CP, Dent JC, Halliwell NA (1996) Particle image velocimetry analysis of IC engine in-cylinder flows. *Opt Lasers Eng* 25:415–432
- Rodi W (1998) Large-eddy simulations of the flow past bluff bodies: state-of-the art. *JSME Ser B* 41:361–374
- Rodi W, Ferziger JH, Breuer M, Pourquie M (1997) Status of large eddy simulation: results of a workshop. *J Fluids Eng* 119:248–263
- Willert CE, Gharib M (1991) Digital particle image velocimetry. *Exp Fluids* 10:181–193